Hindawi
International Journal of Energy Research
Volume 2023, Article ID 8980888, 11 pages
https://doi.org/10.1155/2023/8980888

Research Article

Efficient Electrocatalysts for Hydrogen Evolution Reaction Using Heteroatom-Doped MXene Nanosheet

Mahider Asmare Tekalgne,[1] **Ha Huu Do**,[2] **Tuan Van Nguyen**,[1] **Quyet Van Le**,[1] **Jusung An**,[3] **Sung Hyun Hong**,[1] **Sang Hyun Ahn**,[2] **Heemin Kang**,[1] **Jong Seung Kim**,[3] **and Soo Young Kim**[1]

[1]*Department of Materials Science and Engineering, Korea University, 145 Anam-ro, Seongbuk-gu, Seoul 02841, Republic of Korea*
[2]*School of Chemical Engineering and Materials Science, Chung-Ang University, 84 Heukseok-ro, Dongjak-gu, Seoul 06974, Republic of Korea*
[3]*Department of Chemistry, Korea University, 145 Anam-ro, Seongbuk-gu, Seoul 02841, Republic of Korea*

Correspondence should be addressed to Heemin Kang; heeminkang@korea.ac.kr, Jong Seung Kim; jongskim@korea.ac.kr, and Soo Young Kim; sooyoungkim@korea.ac.kr

Received 2 March 2023; Revised 24 April 2023; Accepted 27 April 2023; Published 10 May 2023

Academic Editor: Sanjay Basumatary

It is crucial to develop a low-cost hybrid electrocatalysts for hydrogen production. Due to their layered structure and strong electrical conductivity, MXene-based materials have been lately used more and more in energy storage devices. Herein, heteroatom- (boron and sulfur-) doped MXene (B, S-$Ti_3C_2T_x$) nanosheets are developed as efficient electrocatalysts for the hydrogen evolution reaction (HER). The synthesized B, S-$Ti_3C_2T_x$ has a large surface area and exhibits excellent electrocatalytic activity in acidic media. The prepared B, S-2-$Ti_3C_2T_x$ catalyst exhibits a low overpotential of −110 mV vs. reversible hydrogen electrode for the HER and a low Tafel slope of ~54 mV dec^{-1}. Furthermore, B, S-2-$Ti_3C_2T_x$ shows a double-layer capacitance of 1.05 mF/cm^2 and maintains a steady catalytic activity for the HER for over 1000 cycles.

1. Introduction

In recent years, hydrogen generation from renewable sources, such as water, has been the focus of research to satisfy the increasing demand for clean energy [1–7]. Electrochemical water splitting is a method used for hydrogen production [8–11]. Because of their excellent hydrogen adsorption, platinum, and its compounds are among the greatest catalysts for hydrogen evolution reaction (HER). This is because of the Gibbs-free energy that they possess [12–14]. However, their high cost and scarcity limit their large-scale applications. Therefore, various materials, including graphene, carbon nanotubes [15], transition-metal dichalcogenides (TMDs) [16–22], transition metal oxides [23, 24], transition-metal carbides (TMCs) [25–29], transition-metal phosphides [29–32], organic polymers [33, 34], and nitrides, have been extensively investigated for replacing expensive Pt-based materials in HER.

Researchers have recently become interested in MXenes, a family of two-dimensional TMCs, notably $Ti_3C_2T_x$ (where the T_x represents the surface functionalization, such as –O, –OH, and –F). Due to the fact that MXenes have a high surface area, great electrical conductivity, and strong chemical and mechanical stabilities [35–37], MXenes have been extensively investigated for use in electrochemical applications such as lithium and sodium ion batteries [38], flexible electrodes [39, 40] as well as supercapacitors [41–43]. Several studies have also been conducted on MXenes as efficient catalysts for HER [44–51]. However, the intrinsic catalytic activity of MXenes is not nearly as strong as that of Pt and TMDs. To further enhance catalytic performance, MXenes have been nanocomposited with various materials, such as

carbonaceous materials, oxides, and metal-organic frameworks [52, 53].

Heteroatom doping of MXene is a promising method for developing efficient electrocatalysts for HER. Recently, Le et al. synthesized nitrogen-doped $Ti_3C_2T_x$, with enhanced electrocatalytic activity toward HER, via heat treatment in an ammonia atmosphere [54]. With an overpotential of 198 mV and a Tafel slope of 92 mV dec^{-1}, the catalyst in its as-obtained state demonstrated strong catalytic activity. Ding et al. studied the HER activities of Ti_2C and Mo_2C doped with nonmetallic heteroatoms such as N, B, P, and S by making use of DFT simulations in their research [55]. All the samples showed a lower Gibbs-free energy than pristine Ti_2C and Mo_2C, indicating their significant potential as HER active catalysts. N-Ti_2CO_2 showed a very small ΔG_H of 0.087 eV and abundant active sites.

Herein, we report $Ti_3C_2T_x$ codoped with boron and sulfur (B, S-$Ti_3C_2T_x$) as an efficient catalyst for electrocatalytic HER. We investigated the catalytic performance of the as-prepared samples at different amounts of the boron precursor. The introduction of boron and sulfur modified the conductivity and increased the active surface area. Specifically, the B, S-2-$Ti_3C_2T_x$ sample exhibited the highest HER performance with a low overpotential of 110 mV compared to the other samples (B, S-1-$Ti_3C_2T_x$ and B, S-3-$Ti_3C_2T_x$). This improved performance was attributed to the synergistic contributions of boron- and sulfur-coordinated species.

2. Experimental

2.1. Materials. Boric acid (99.5%), thiourea (99.0%), LiF, H_2SO_4 (98%), and Nafion solution (5 wt%) were purchased from Sigma-Aldrich. Pristine Ti_3AlC_2 (99.8%, 300 mesh) was purchased from Forsman Scientific Beijing Co., Ltd., China. HCl was supplied by Daejeong.

2.2. Synthesis of $Ti_3C_2T_x$. To obtain $Ti_3C_2T_x$ MXene, the starting material Ti_3AlC_2 (MAX) was subjected to an etching process where the Al layer was removed using a LiF/HCl solution. A solution for etching was prepared by adding 0.8 g of LiF to a 30 mL HCl solution, followed by stirring. 1 g of Ti_3AlC_2 (MAX) powder was then added to the etching solution at 40°C and reacted for 24 hours until the Al layer was completely removed. The bulk $Ti_3C_2T_x$ MXene was collected by centrifugation, washed with deionized (DI) water to achieve a final pH of about 6, and then dried under vacuum overnight at 60°C.

2.3. Synthesis of B-Doped $Ti_3C_2T_x$. A simple hydrothermal procedure was used to fabricate B-doped $Ti_3C_2T_x$ specimens. 100 mg $Ti_3C_2T_x$ and various concentrations of boric acid (0.75, 1.5, and 3 g) were typically added to 60 mL of DI water and mixed for 1 hour at room temperature. The solution was then placed into a Teflon-lined autoclave reactor and hydrothermally heated for 24 hours at 180°C. The centrifuged suspension was rinsed with DI water and dried at 80°C for 12 hours. The as-prepared B-doped specimens were labeled B-1-$Ti_3C_2T_x$, B-2-$Ti_3C_2T_x$, and B-3-$Ti_3C_2T_x$, corresponding to 0.75, 1.5, and 3 g of boric acid precursor, respectively.

2.4. Synthesis of S-Doped $Ti_3C_2T_x$. S-doped $Ti_3C_2T_x$ was synthesized using thiourea as the sulfur source. 100 mg of $Ti_3C_2T_x$ powder and 1.2 g of thiourea were added to 60 mL of DI water and mixed at room temperature for one hour. The solution was then placed into the Teflon-lined autoclave reactor and hydrothermally heated for 24 hours at 180°C. S-$Ti_3C_2T_x$ was collected by centrifugation, rinsed with DI water, and dried in a vacuum oven at 80°C for 12 hours.

2.5. Synthesis of B, S-$Ti_3C_2T_x$. B, S-$Ti_3C_2T_x$ was successfully synthesized through a single-step reaction. $Ti_3C_2T_x$ (100 mg), thiourea (1.2 g), and different amounts of boric acid (0.75, 1.5, or 3 g) were dissolved in 60 mL of DI water with continuous magnetic stirring for 1 h at room temperature. The solution was then placed into an autoclave reactor coated with Teflon and hydrothermally heated at 180°C for 24 hours. The resulting specimens (designated as B, S-1-$Ti_3C_2T_x$, B, S-2-$Ti_3C_2T_x$, and B, S-3-$Ti_3C_2T_x$) were obtained via centrifugation and drying at 80°C for 12 h.

2.6. Materials Characterization. The crystal structure of the synthesized specimens was studied via X-ray diffraction (XRD; Bruker New D8-Advance, Seoul, Korea) using Cu Kα radiation ($\lambda = 0.154$ nm). Raman spectra were obtained using a Raman spectrometer (LabRAM-HR Evolution). Field-emission scanning electron microscopy (FE-SEM; Zeiss 300 VP, Seoul, Korea) images were obtained at an acceleration voltage of 10 kV to study the morphology of the as-prepared samples. Transmission electron microscopy (TEM; JEOL-2100F) was conducted to further confirm the morphology. The X-ray photoelectron spectroscopy (XPS) technique was applied to verify the elemental build of the catalysts as well as the oxidation states of the constituent elements.

2.7. Electrochemical Measurements. All electrochemical measurements were carried out at room temperature using an Ivium potentiostat V55630 and a typical three-electrode electrolytic setup. As the reference, counter, and working electrodes, respectively, the saturated calomel electrode (SCE), graphite rod, and B, S-$Ti_3C_2T_x$ on a glassy electrode were used. At a scan rate of 5 mV s1, linear sweep voltammetry (LSV) was used to measure the HER activity. Each and every measurement was carried out in 0.5 M H_2SO_4 while iR compensation was used. To determine the level of stability, continuous cyclic voltammograms were obtained at a scan rate of 50 mV s^{-1} for a total of 1000 cycles. In addition, electrochemical impedance spectroscopy, known as EIS, was carried out at a potential of -230 mV vs. RHE and at frequencies ranging from 100 kHz to 0.1 Hz. Using the following equation, each potential was correlated to the RHE to ensure accuracy:

$$E(RHE) = E(SCE) + 0.2\ V + 0.059\,pH. \quad (1)$$

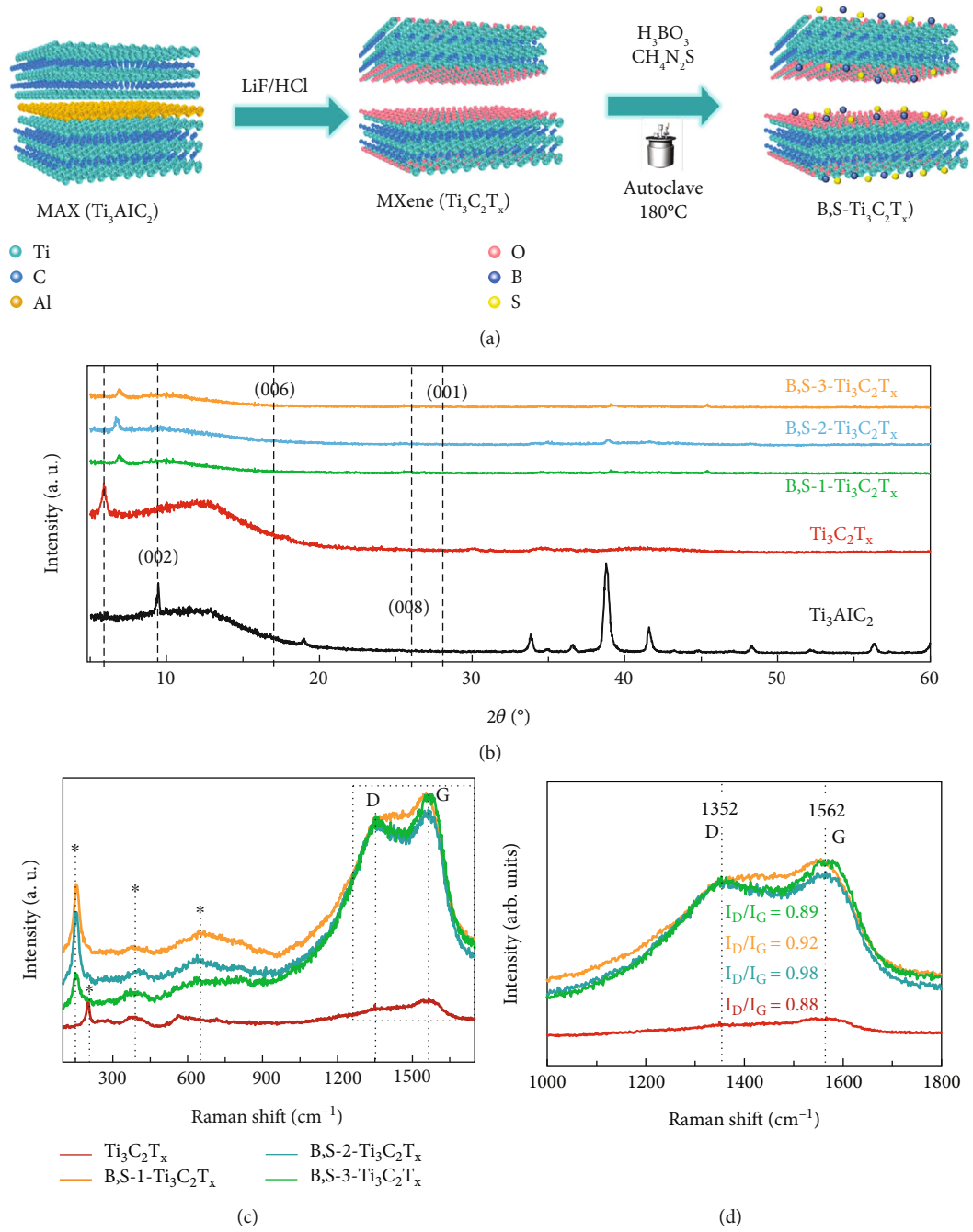

Figure 1: (a) Schematic illustration of the synthesis procedure of B, S-$Ti_3C_2T_x$. Ti_3AlC_2 was used as the precursor for the preparation of $Ti_3C_2T_x$, of which was then autoclaved to result in B, S-$Ti_3C_2T_x$. (b) X-ray diffraction (XRD) data showing the crystal structures. (c, d) Raman spectra showing the chemical compositions as well as the origin of disordered carbon of as-synthesized $Ti_3C_2T_x$ and B, S-$Ti_3C_2T_x$ samples.

3. Results and Discussion

Figure 1(a) shows the procedure for preparing B, S-$Ti_3C_2T_x$. Ti_3AlC_2 was used as the precursor in the preparation of Ti_3C_2Tx. The B, S-$Ti_3C_2T_x$ hybrid was fabricated through a simple hydrothermal method. The crystal structure of the bare Ti_3AlC_2, $Ti_3C_2T_x$ MXene, and B, S-$Ti_3C_2T_x$ was analyzed using XRD (Figure 1(b)). The peaks of the bare $Ti_3C_2T_x$ corresponding to (002), (006), (008), and (001) were observed, consistent with previous finding [42]. The basal plane peaks of $Ti_3C_2T_x$ shifted to 5.8° from 9.4° for the Ti_3AlC_2 precursors, indicating a widening of d-spacings due to Al removal [56, 57]. These peaks slightly shifted to lower angles after the addition of B and S, but other peaks remained, albeit with decreasing intensities as the doping concentration increased. Raman spectroscopy (Figure 1(c)) was utilized to determine the chemical composition of B, S-$Ti_3C_2T_x$ and the origin of disordered carbon.

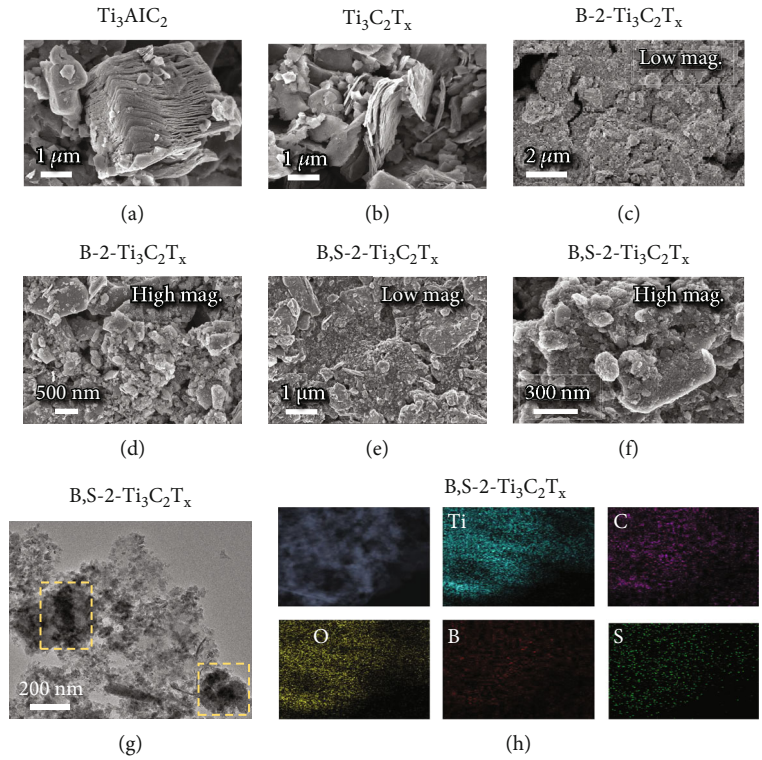

Figure 2: Field-emission scanning electron microscopy (FE-SEM) images showing the morphologies of (a) Ti_3AlC_2 parent phase, (b) pristine $Ti_3C_2T_x$, (c) B-2 – $Ti_3C_2T_x$ in low magnification, (d) B-2 – $Ti_3C_2T_x$ in high magnification, (e) B, S-2-$Ti_3C_2T_x$ in low magnification, and (f) B, S-2-$Ti_3C_2T_x$ in high magnification. (g) Transmission electron microscopy (TEM) images and (h) high-angle annular dark field scanning TEM (HAADF-STEM) as well as energy dispersive X-ray spectroscopy (EDX) elemental maps of B, S-2-$Ti_3C_2T_x$.

In addition to the D and G bands at 1352 cm^{-1} and 1562 cm^{-1}, respectively, all B, S-$Ti_3C_2T_x$ MXene samples and pristine MXene exhibited signals of nonstoichiometric titanium carbide and anatase phases of titanium oxide at 199, 381, and 642 cm^{-1} (G band) [58]. The I_D/I_G ratio, which compares the intensities of the D and G bands, is commonly used in order to conduct an assessment of the defect formation. The I_D/I_G gradually increases (from 0.92 to 0.98) as the boric acid dosage increases from 0.75 to 1.5 g (Figure 1(d)), indicating larger defects and the substitution of carbon atoms in $Ti_3C_2T_x$ by boron/sulfur, which could improve the performance of electrochemical measurement of the material.

The morphology of Ti_3AlC_2, $Ti_3C_2T_x$, B-2-$Ti_3C_2T_x$, and B, S-2-Ti_3C_2Tx was observed using FE-SEM at high and low magnifications (Figures 2(a)–2(f)). The successful etching of aluminum was confirmed by the observation of multilayered $Ti_3C_2T_x$ in Figure 2(b). Figure 2(g) shows a high-resolution TEM image of B, S-2-$Ti_3C_2T_x$ at 200 nm magnification, with the dashed frames indicating the aggregated B and S doped on the $Ti_3C_2T_x$ nanosheet.

To verify the morphology and interlayer distance as well as the corresponding plane, TEM analysis was carried out. The high-resolution TEM image of B, S-2-$Ti_3C_2T_x$ is shown in Figure S1(a-c) (supporting information), with a magnification range of 50 to 200 nm. Crystal defects were observed in B, S-2-$Ti_3C_2T_x$ enclosed by a yellow dashed line, which can be explained by the substitution of B and S for the C sites. To confirm the successful preparation of B, S-2-$Ti_3C_2T_x$, EDX elemental mapping was taken of a specific area (Figure 2(h)). The elements B, S, Ti, C, and O were uniformly dispersed.

We used XPS to verify the successful synthesis of $Ti_3C_2T_x$ as well as the existence of constituent atoms in B, S-2-$Ti_3C_2T_x$ and B-2-$Ti_3C_2T_x$ (Figures S2 and S3). The fact that the survey scan revealed the presence of titanium, carbon, oxygen, and boron is evidence that the $Ti_3C_2T_x$ and B, S-2-$Ti_3C_2T_x$ MXenes were successfully prepared. This is illustrated in Figure 3(a). On the other hand, S is not easily discernible in the survey scan, which leads one to believe that the amount of S that was doped into the sample was quite low. As a result of this, high-resolution XPS scans were carried out in order to obtain additional confirmation that B and S were present in the sample. High-resolution Ti 2p spectra of $Ti_3C_2T_x$ can be divided into four peaks at 455.3, 456.1, 457.3, and 458.8 eV, which are attributed to Ti–C, Ti^{2+}, Ti^{3+}, and Ti–O, respectively (Figure 3(a)), as previously reported [59]. Compared with the $Ti_3C_2T_x$ sample, a smaller-intensity peak of Ti–C at 454.9 eV and a peak shift of 0.4 eV are observed, whereas a stronger peak of Ti–O appears at 458.7 eV in the B-$Ti_3C_2T_x$ MXene sample (Figure. S4(a)). Based on previous reports, the presence of Ti^{3+} in B-$Ti_3C_2T_x$, which is formed through the reduction of Ti^{4+}, leads to electron transfer from Ti to B and produces a B–Ti–O substitutional site

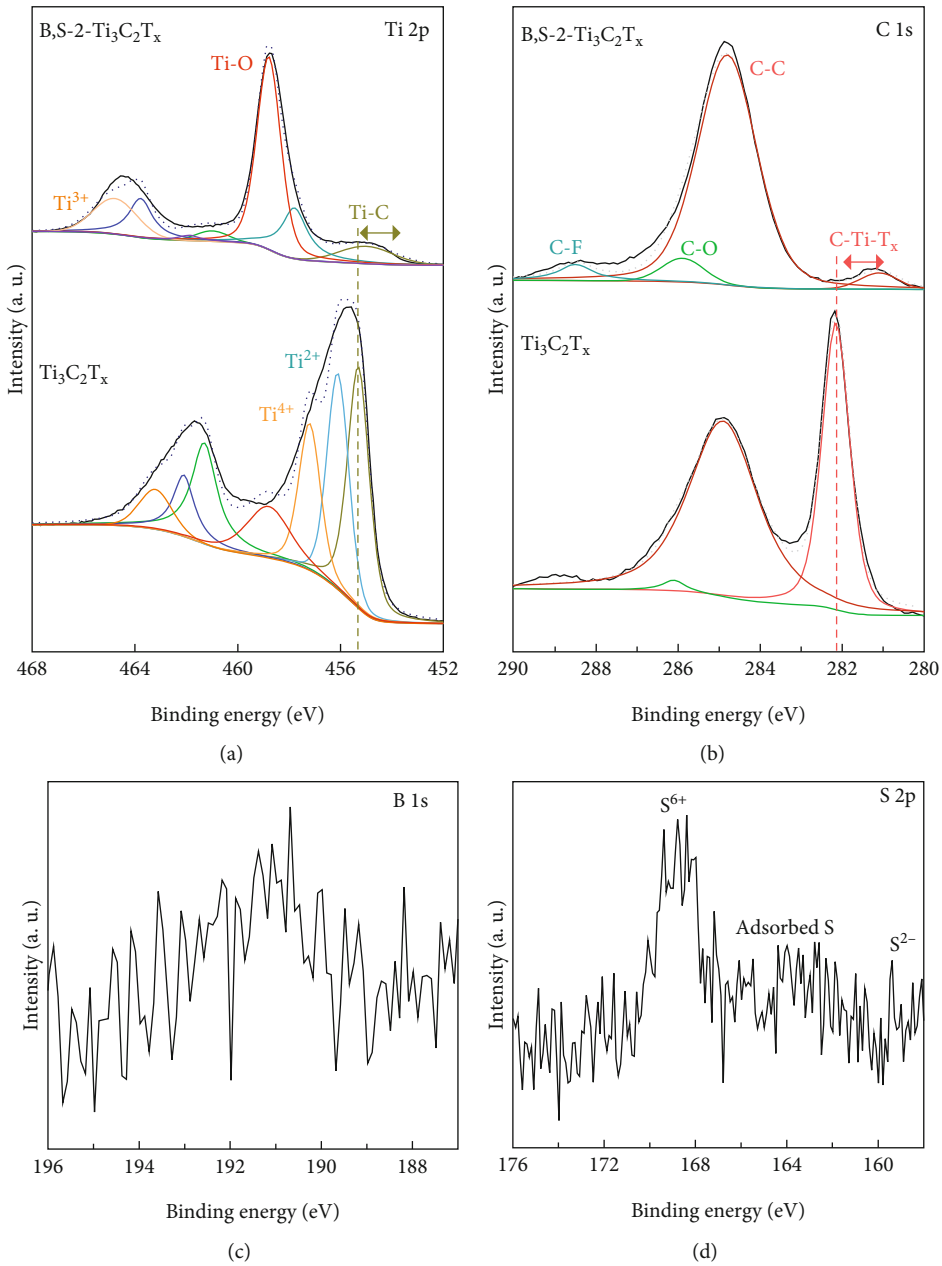

Figure 3: Successful synthesis of $Ti_3C_2T_x$ confirmed by (a) high-resolution X-ray photoelectron spectroscopy (XPS) spectra of Ti 2p and (b) high-resolution XPS spectra of C 1 s in $Ti_3C_2T_x$. Successful synthesis of B, S-2-$Ti_3C_2T_x$ was confirmed via (c) XPS spectra of B 1 s and (d) XPS spectra of S 2p in B, S-2-$Ti_3C_2T_x$.

[60–62]. The Ti 2p spectra of B, S-$Ti_3C_2T_x$ confirm the presence of Ti^{2+} and Ti–O at 457.8 and 458.8 eV, respectively. Moreover, the Ti–C peak is difficult to distinguish from the Ti–S signal because of spectral overlap at ~455.1 eV [63]. The C–Ti, C–C, and C–O bonds of $Ti_3C_2T_x$ are observed in the high-resolution C 1 s spectrum at 282.1, 284.9, and 285.9 eV, respectively (Figure 3(b)). The C–C component of B, S-$Ti_3C_2T_x$ is observed at 284.8 eV, which is ~0.2 eV higher than the energy of the C–C component of B-$Ti_3C_2T_x$ (Figure. S4(b)) possibly because of the chemical interaction between S and the surrounding atoms in B-$Ti_3C_2T_x$.

Additionally, the C 1 s spectra exhibit the presence of C–Ti (281.1 eV), C–C (284.7 eV), and C–O (285.8 eV) bonds (Figure 3(b)). Moreover, the high-resolution C 1 s XPS spectrum of B-$Ti_3C_2T_x$ shows peaks at 281.1, 284.6, 285.9, and 283.9 eV, which are assigned to C–Ti, C–C, and C–B bonds, respectively (Figure. S4(b)). For O 1 s spectra, a single peak appears at 529.9 eV for B-$Ti_3C_2T_x$, which can be deconvoluted into four peaks for O–Ti–C (530.1 eV), H–O–Ti (531 eV), O–C (532.2), and B–O–B (533.1 eV) bonds (Figure S5). Only three peaks belonging to O–Ti, H–O–Ti, and O–C are observed in $Ti_3C_2T_x$, implying the presence of B–O in B-Ti_3C_2Tx. Boron

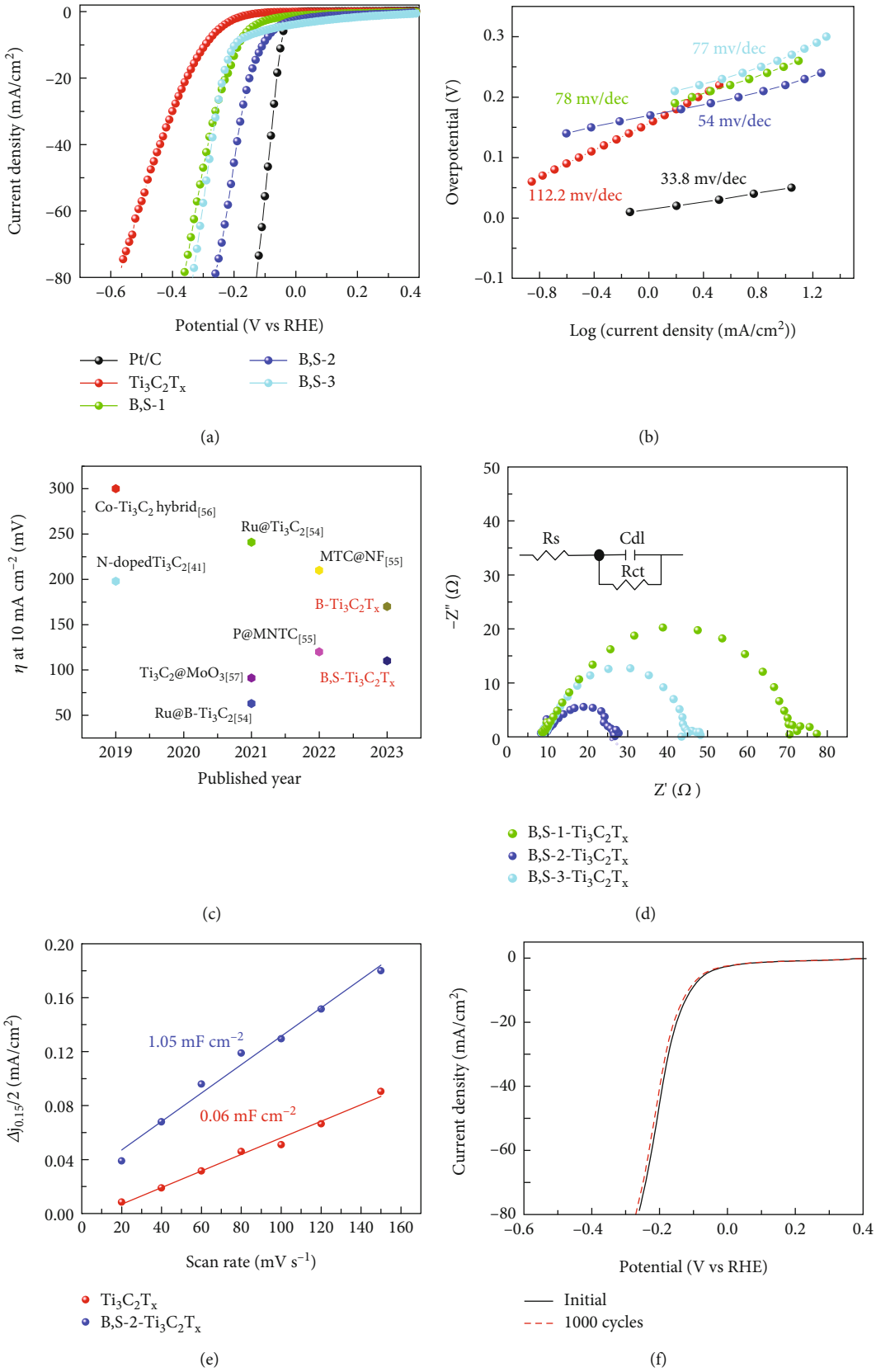

Figure 4: (a) LSV curves and (b) Tafel plots of the as-prepared catalysts. (c) Comparison of the overpotential required to achieve a current density of 10 mA/cm^2. (d) EIS spectra of B, S-$Ti_3C_2T_x$ at −0.3 V vs. RHE in 0.5 M H_2SO_4 (inset: equivalent circuit). (e) double-layer capacitance (c_{dl}) of $Ti_3C_2T_x$ and B, S-$Ti_3C_2T_x$ electrocatalysts at 0.15 V vs. RHE as a function of the scan rate. (f) polarization curves of B, S-$Ti_3C_2T_x$ catalysts before and after 1000 CV cycles (at a scan rate of 50 mV s^{-1}) in 0.5 M H_2SO_4.

doping is confirmed in the B 1 s spectra at 190.6 eV (Figure 3(c)). The boron content in B, S-2-Ti_3C_2Tx is approximately 5% with a sulfur content of less than 1% in atomic ratio. The S 2p spectrum reveals the binding energy of S^{2-} by showing two peaks of S^{2-}1/2 at 168.7 and S 2p3/2 at 162.7 eV (Figure 3(d)). Additionally, in the B 1 s spectra of B-$Ti_3C_2T_x$ (Figure. S6), peaks are observed at binding energies of 192 and 193.3 eV, corresponding to B–O–Ti and B–O–B, respectively [64, 65].

The electrochemical analyses were conducted using a three-electrode system to evaluate the HER catalytic properties of the Ti_3C_2Tx, B-$Ti_3C_2T_x$, and B, S-$Ti_3C_2T_x$ electrocatalysts in 0.5 M of H_2SO_4. The commercial Pt/C catalyst was employed as a reference, and it demonstrates the highest HER activity, with practically zero onset potential and low overpotential (at10 mA cm^{-2}), in contrast to the pristine $Ti_3C_2T_x$ catalyst, which demonstrates a significantly lower level of catalytic activity [66]. Initially, the B-doped $Ti_3C_2T_x$ catalysts were examined for their properties (Table S1). The B-2-$Ti_3C_2T_x$ catalyst displayed a level of activity that was noticeably higher than that of the other catalysts. Specifically, B-2-Ti_3C_2Tx shows an overpotential of 170 mV (at 10 mA cm^{-2}), whereas B-1-$Ti_3C_2T_x$ and B-3-$Ti_3C_2T_x$ exhibit overpotentials of 250 and 220 mV, respectively (Figure. S7(a)). Their electrocatalytic performances are compared in Figure. S7(b) based on the potential obtained at a constant current density of 10 mA cm^{-2}. We believe that the synergistic effects of active sites on Ti–C, B–O–B, and B–O–Ti species are responsible for the improvement in HER reactivity that we observed following B-doping. The corresponding Tafel slopes of the as-prepared catalysts, which can provide information about the mechanism of HER electrocatalysis, were calculated to be 112.2, 98, 64, and 80 mV dec1 for pristine $Ti_3C_2T_x$, B-1-$Ti_3C_2T_x$, B-2-$Ti_3C_2T_x$, and B-3-$Ti_3C_2T_x$, respectively; B-2- $Ti_3C_2T_x$ has the lowest Tafel slope (Figure. S8(a)).

We also investigated the S-doped $Ti_3C_2T_x$ catalyst (Table S2). S-$Ti_3C_2T_x$ exhibits significantly higher activity than pristine $Ti_3C_2T_x$ (Figure S9(a)). Specifically, it shows an overpotential of 230 mV (at 10 mA cm^{-2}), whereas $Ti_3C_2T_x$ exhibits an overpotential of 300 mV (Figure S9(b)). The corresponding Tafel slopes are calculated to be 86.6 mV dec^{-1} (Figure S9(c)). Our goal was to achieve maximum HER activity by adjusting the concentration of the boron precursor on the surface of the MXene. It may come as a surprise, but the overpotential of B-2-$Ti_3C_2T_x$ at 10 mA cm^{-2} is just 170 mV. This value is significantly lower than that of B-1-$Ti_3C_2T_x$. If the catalytic activity of B-doped electrocatalysts was exclusively dependent on the B–O–Ti composition, then B-3-$Ti_3C_2T_x$ with a greater B-doping content would demonstrate higher performance than B-2-$Ti_3C_2T_x$. This finding, on the other hand, demonstrates that additional interactions, such as O-Ti-C, also contribute to the improvement in catalytic activity. This also suggests that the optimal quantity of the B precursor is critical for achieving the highest possible level of HER activity from the catalyst.

To further enhance the HER kinetics of B-doped catalysts, S was added to the as-prepared catalyst, and the catalytic activity was investigated. The introduction of S significantly improved the catalytic performances of the catalysts. B-2-$Ti_3C_2T_x$ shows an overpotential of 170 mV at a current density of 10 mA cm^{-2}; at the same time, B, S-2-$Ti_3C_2T_x$ catalyst exhibits a significantly lower overpotential (110 mV) than both B-$Ti_3C_2T_x$ and S-$Ti_3C_2T_x$, demonstrating the synergistic effect of the dual-heteroatom doping of 2D $Ti_3C_2T_x$ nanosheets (Figure 4(a)). Similarly, B, S-2-$Ti_3C_2T_x$ and B, S-3-$Ti_3C_2T_x$ exhibit overpotentials (at 10 mA cm^{-2}) of 180 and 200 mV, respectively, which are lower than that of B-$Ti_3C_2T_x$. In their work, Le et al. investigated the kinetics and electronic behavior of doped MXene [54]. DFT calculations were carried out, and the electronic band structure and charge difference for hydrogen adsorption of the Ru@B-Mxene are illustrated. The calculated values of $\Delta G_H{}^*$ for atomic H adsorption on the Ru@B-Mxene compared to the nondoped MXene are low, which plays a crucial role in reducing the charge-transfer resistance of the 2D MXene nanosheet for the HER. The Tafel slopes of B, S-1-$Ti_3C_2T_x$, B, S-2-$Ti_3C_2T_x$, and B, S-3-$Ti_3C_2T_x$ are 78, 54, and 77 mV dec^{-1}, respectively, which are lower than those of the respective B-doped $Ti_3C_2T_x$ specimens, signifying faster HER kinetics (Figure 4(b)). The figure (Figure 4(c)) shows a comparison of overpotential at 10 mA/cm^2 with other reported MXene electrocatalysts [54, 67–70]. In addition, the electrocatalytic performance based on the potential obtained at a constant current density of 10 mA cm^{-2} of the prepared catalyst is shown in Figure. S10.

EIS measurements were conducted to further study the kinetics of the catalyst for HER. The EIS plots in Figure 4(d) show that the charge-transfer resistance (R_{ct}) of an electrode, represented by the semicircle, significantly decreases after B and S doping of $Ti_3C_2T_x$. Consequently, the Rct of B, S-2-$Ti_3C_2T_x$ is significantly smaller than that of B-2-$Ti_3C_2T_x$. This confirms the higher rate of charge transport in the B and S codoped MXenes.

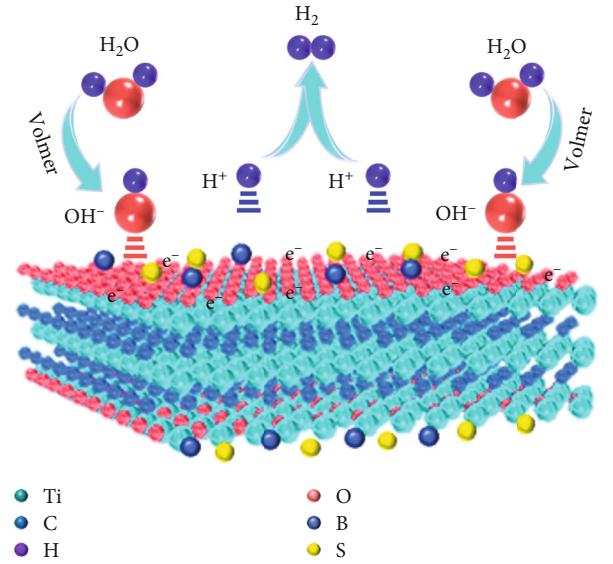

Figure 5: Schematic illustration of the HER catalysis mechanism for B, S-$Ti_3C_2T_x$ in an acidic medium.

B, S-1-$Ti_3C_2T_x$ and B, S-3-$Ti_3C_2T_x$ samples exhibit resistances of 70 and 40 Ω, respectively. Moreover, B-2-$Ti_3C_2T_x$ shows an Rct of 60 Ω, which is lower than those of B-1-$Ti_3C_2T_x$ (80 Ω) and B-2-$Ti_3C_2T_x$ (100 Ω), as shown in Figure S9(b). This result is in perfect agreement with the results obtained from the LSV and Tafel plots, which suggest that HER possesses excellent electrocatalytic activity.

CV curves at scan rates of 20–150 mV s^{-1} were used to determine the Cdl (Figure S11). The Cdl of B, S-2-$Ti_3C_2T_x$ is 1.05 mF cm^{-2} (Figure 4(e)). The enhanced catalytic performance of B, S-$Ti_3C_2T_x$ can be attributed to the high conductivity of B, S-$Ti_3C_2T_x$, which enables fast charge transfer and increases the number of active sites, allowing the faster reduction of adsorbed hydrogen ions.

Long-time stability is an important parameter for the catalysts. Therefore, long-term cycling tests of B, S-2-$Ti_3C_2T_x$ were conducted for 1000 cycles in an acidic medium. As shown in Figure 4(f), the sample does not show significant differences before and after cycling, indicating that the B, S-2-$Ti_3C_2T_x$ catalyst has excellent HER activity with long-term stability. Additionally, the electrochemical surface area of the prepared samples was estimated using double-layer capacitance (C_{dl}) to investigate whether the number of active sites has increased after the incorporation of B and S.

Based on the obtained HER performance of B, S-$Ti_3C_2T_x$, an electrocatalytic mechanism has been proposed, as shown in Figure 5. This process occurs at the surface. Boron, sulfur, and Ti_3C_2, with their unique advantages, play specific roles in different elementary reactions to synergistically improve the HER kinetics.

4. Conclusions

B, S-$Ti_3C_2T_x$ MXenes were fabricated via a facile one-step hydrothermal process. B, S-$Ti_3C_2T_x$ showed excellent electrocatalytic HER performance compared to pristine $Ti_3C_2T_x$. Specifically, the B, S-2-$Ti_3C_2T_x$ catalyst exhibited high catalytic activity with a low overpotential of 110 mV at 10 mA cm^{-2} for HER and excellent stability over 1000 continuous CV cycles. Therefore, this study demonstrates a promising strategy for the metal-free codoping of MXene nanosheets.

Data Availability

The data used to support the findings of this study are included within the manuscript and the supplementary information files.

Conflicts of Interest

The authors declare that they have no conflicts of interest.

Authors' Contributions

Mahider Asmare Tekalgne and Ha Huu Do contributed equally to this work.

Acknowledgments

This research was supported by the NRF funded by the Korean government (2021R1A4A3027878 and 2022M3H4A1A01012712) and CRI project (no. 2018R1A3B1052702).

Supplementary Materials

Figure S1: TEM images of B, S-$Ti_3C_2T_x$. Figure S2: XPS survey spectra of $Ti_3C_2T_x$ and B, S-$Ti_3C_2T_x$. Figure S3: XPS survey spectra of B-2-$Ti_3C_2T_x$. Figure S4: high-resolution XPS of B-2-$Ti_3C_2T_x$. Figure S5: high-resolution XPS spectra of O 1 s in $Ti_3C_2T_x$ and B, S-2-$Ti_3C_2T_x$. Figure S6: B 1 s spectrum of B-2-$Ti_3C_2T_x$ nanosheet. Figure S7: LSV and overpotential values B-$Ti_3C_2T_x$. Figure S8: Tafel plot and EIS spectra of B-$Ti_3C_2T_x$. Figure S9: LSV, overpotential values, and Tafel plot of S-$Ti_3C_2T_x$. Figure S10: overpotential values of B, S-$Ti_3C_2T_x$. Figure S11: CV curves of $Ti_3C_2T_x$ and B, S-$Ti_3C_2T_x$. Table S1: overpotential values of $Ti_3C_2T_x$ and B-$Ti_3C_2T_x$. Table S2: overpotential values of S-$Ti_3C_2T_x$ and B, S-$Ti_3C_2T_x$. (Supplementary Materials). *(Supplementary Materials)*

References

[1] M. Cabán-Acevedo, M. L. Stone, J. Schmidt et al., "Efficient hydrogen evolution catalysis using ternary pyrite-type cobalt phosphosulphide," *Nature Materials*, vol. 14, no. 12, pp. 1245–1251, 2015.

[2] Y. Zheng, Y. Jiao, Y. Zhu et al., "Hydrogen evolution by a metal-free electrocatalyst," *Nature Communications*, vol. 5, no. 1, pp. 1–8, 2014.

[3] Q. Wang, F. Mi, J. Li et al., "Tungsten doping generated Mo_2C-MoC heterostructure to improve HER performance in alkaline solution," *Electrochimica Acta*, vol. 370, article 137796, 2021.

[4] M. Dresselhaus and I. Thomas, "Alternative energy technologies," *Nature*, vol. 414, no. 6861, pp. 332–337, 2001.

[5] J. A. Turner, "Sustainable hydrogen production," *Science*, vol. 305, no. 5686, pp. 972–974, 2004.

[6] Z. Chen, X. Duan, W. Wei, S. Wang, and B.-J. Ni, "Recent advances in transition metal-based electrocatalysts for alkaline hydrogen evolution," *Journal of Material Chemistry A*, vol. 7, no. 25, pp. 14971–15005, 2019.

[7] B. You, M. T. Tang, C. Tsai, F. Abild-Pedersen, X. Zheng, and H. Li, "Enhancing electrocatalytic water splitting by strain engineering," *Advanced Materials*, vol. 31, no. 17, article 1807001, 2019.

[8] T. Ouyang, Y. Q. Ye, C. Y. Wu, K. Xiao, and Z. Q. Liu, "Heterostructures composed of N-doped carbon nanotubes encapsulating cobalt and β-Mo_2C nanoparticles as bifunctional electrodes for water splitting," *Angewandte Chemie International Edition*, vol. 131, no. 15, pp. 4977–4982, 2019.

[9] S. Kim, K. H. Kim, C. Oh, K. Zhang, and J. H. Park, "Artificial photosynthesis for high-value-added chemicals: old material, new opportunity," *Carbon Energy*, vol. 4, no. 1, pp. 21–44, 2022.

[10] P. Kuang, M. He, H. Zou, J. Yu, and K. Fan, "0D/3D MoS_2-NiS_2/N-doped graphene foam composite for efficient overall

water splitting," *Applied Catalysis B: Enviromental*, vol. 254, pp. 15–25, 2019.

[11] H. H. Do, T. D. C. Ha, H. Jo et al., "Low-temperature synthesis of molybdenum sulfides, tungsten sulfides, and composites thereof as efficient electrocatalysts for hydrogen evolution reaction," *Applied Surface Science*, vol. 576, article 151828, 2022.

[12] D. Kobayashi, H. Kobayashi, D. Wu et al., "Significant enhancement of hydrogen evolution reaction activity by negatively charged Pt through light doping of W," *Journal of American Chemical Society*, vol. 142, no. 41, pp. 17250–17254, 2020.

[13] Y. Shi, Z.-R. Ma, Y.-Y. Xiao et al., "Electronic metal-support interaction modulates single-atom platinum catalysis for hydrogen evolution reaction," *Nature Communications*, vol. 12, no. 1, pp. 1–11, 2021.

[14] Z. Li, R. Ge, J. Su, and L. Chen, "Recent progress in low Pt content electrocatalysts for hydrogen evolution reaction," *Advanced Materials Interfaces*, vol. 7, no. 14, article 2000396, 2020.

[15] S.-H. Lee, J. H. Park, and S. Kim, "Synthesis, property, and application of carbon nanotube fiber," *Journal of the Korean Ceramic Society*, vol. 58, no. 2, pp. 148–159, 2021.

[16] Z. Liu, Z. Gao, Y. Liu, M. Xia, R. Wang, and N. Li, "Heterogeneous nanostructure based on 1T-phase MoS_2 for enhanced electrocatalytic hydrogen evolution," *ACS Applied Material Interfaces*, vol. 9, no. 30, pp. 25291–25297, 2017.

[17] X. Xue, J. Zhang, I. A. Saana, J. Sun, Q. Xu, and S. Mu, "Rational inert-basal-plane activating design of ultrathin 1T′ phase MoS_2 with a MoO_3 heterostructure for enhancing hydrogen evolution performances," *Nanoscale*, vol. 10, no. 35, pp. 16531–16538, 2018.

[18] P. Prabhu, V. Jose, and J.-M. Lee, "Design strategies for development of TMD-based heterostructures in electrochemical energy systems," *Journal of Korean Ceramic Society*, vol. 2, no. 3, pp. 526–553, 2020.

[19] H. Wang, X. Xiao, S. Liu et al., "Structural and electronic optimization of MoS_2Edges for hydrogen evolution," *Journal of American Chemical Society*, vol. 141, no. 46, pp. 18578–18584, 2019.

[20] Q. Zhou, Z. Chen, L. Zhong et al., "Solvothermally controlled synthesis of organic–inorganic hybrid nanosheets as efficient pH-universal hydrogen-evolution electrocatalysts," *ChemSusChem*, vol. 11, no. 16, pp. 2828–2836, 2018.

[21] Q. Zhou, J. Feng, X. Peng, L. Zhong, and R. Sun, "Porous carbon coupled with an interlaced MoP-MoS_2 heterojunction hybrid for efficient hydrogen evolution reaction," *Journal of Energy Chemistry*, vol. 45, pp. 45–51, 2020.

[22] Q. Zhou, Z. Yao, H. Wang et al., "Interface engineering of Ni_xS_y@MoS_2 heterostructured nanorods as high-efficient electrocatalysts for water splitting," *International Journal of Hydrogen Energy*, vol. 46, no. 71, pp. 35077–35087, 2021.

[23] B. Jin, Y. Cho, C. Park et al., "A two-photon tandem black phosphorus quantum dot-sensitized $BiVO_4$ photoanode for solar water splitting," *Energy & Environmental Science*, vol. 15, no. 2, pp. 672–679, 2022.

[24] K. H. Kim, C. W. Choi, S. Choung et al., "Continuous oxygen vacancy gradient in TiO_2 photoelectrodes by a photoelectrochemical-driven "self-purification" process," *Advanced Energy Materials*, vol. 12, no. 7, article 2103495, 2022.

[25] H. Vrubel and X. Hu, "Molybdenum boride and carbide catalyze hydrogen evolution in both acidic and basic solutions," *Angewantde Chemie International Edition*, vol. 51, no. 51, pp. 12703–12706, 2012.

[26] W.-F. Chen, C.-H. Wang, K. Sasaki et al., "Highly active and durable nanostructured molybdenum carbide electrocatalysts for hydrogen production," *Energy Enviromental Science*, vol. 6, no. 3, pp. 943–951, 2013.

[27] H. Wang and J.-M. Lee, "Recent advances in structural engineering of MXene electrocatalysts," *Journal of Material Chemistry A*, vol. 8, no. 21, pp. 10604–10624, 2020.

[28] H. Wang, Y. Lin, S. Liu et al., "Confined growth of pyridinic N–Mo_2C sites on MXenes for hydrogen evolution," *Journal of Material Chemistry A*, vol. 8, no. 15, pp. 7109–7116, 2020.

[29] F. H. Saadi, A. I. Carim, E. Verlage, J. C. Hemminger, N. S. Lewis, and M. P. Soriaga, "CoP as an acid-stable active electrocatalyst for the hydrogen-evolution reaction: electrochemical synthesis, interfacial characterization and performance evaluation," *Journal of Physical Chemistry C*, vol. 118, no. 50, pp. 29294–29300, 2014.

[30] H. Du, R. M. Kong, X. Guo, F. Qu, and J. Li, "Recent progress in transition metal phosphides with enhanced electrocatalysis for hydrogen evolution," *Nanoscale*, vol. 10, pp. 21617–21624, 2018.

[31] E. J. Popczun, C. G. Read, C. W. Roske, N. S. Lewis, and R. E. Schaak, "Highly active electrocatalysis of the hydrogen evolution reaction by cobalt phosphide nanoparticles," *Angewantde Chemie International Edition*, vol. 53, no. 21, pp. 5427–5430, 2014.

[32] P. Xiao, M. A. Sk, L. Thia et al., "Molybdenum phosphide as an efficient electrocatalyst for the hydrogen evolution reaction," *Energy Enviromental Science*, vol. 7, no. 8, pp. 2624–2629, 2014.

[33] B. C. Patra, S. Khilari, R. N. Manna et al., "A metal-free covalent organic polymer for electrocatalytic hydrogen evolution," *ACS Catalysis*, vol. 7, no. 9, pp. 6120–6127, 2017.

[34] S. Chatterjee, S. Shaymal, M. Mukherjee et al., "Metal-thiolate framework for electrochemical and Photoelectrochemical hydrogen generation," *ChemSusChem*, vol. 15, no. 10, article e202200114, 2022.

[35] M. R. Lukatskaya, S. Kota, Z. Lin et al., "Ultra-high-rate pseudocapacitive energy storage in two-dimensional transition metal carbides," *Energy Storage Materials*, vol. 2, no. 8, pp. 1–6, 2017.

[36] S. Wang, Y. Du, W. Liao, and Z. Sun, "Hydrogen adsorption, dissociation and diffusion on two-dimensional Ti_2C monolayer," *International Journal of Hydrogen Energy*, vol. 42, no. 44, pp. 27214–27219, 2017.

[37] B. Anasori, M. R. Lukatskaya, and Y. Gogotsi, "2D metal carbides and nitrides (MXenes) for energy storage," *Nature Reviews Materials*, vol. 2, no. 2, pp. 1–17, 2017.

[38] X. Liang, A. Garsuch, and L. F. Nazar, "Sulfur cathodes based on conductive MXene nanosheets for high-performance lithium–sulfur batteries," *Angewandte Chemie International Edition*, vol. 127, no. 13, pp. 3979–3983, 2015.

[39] J. S. Meena, S. B. Choi, and J.-W. Kim, "Review on Ti_3C_2-based MXene Nanosheets for flexible electrodes," *Electronic Materials Letters*, vol. 18, no. 3, pp. 256–274, 2022.

[40] H.-S. Lim, S. B. Choi, H. Kwon et al., "Development of a highly flexible composite electrode comprised of Ti_3C_2-based MXene nanosheets and ag nanoparticles," *Electronic Materials Letters*, vol. 17, no. 6, pp. 513–520, 2021.

[41] M. R. Lukatskaya, O. Mashtalir, C. E. Ren et al., "Cation intercalation and high volumetric capacitance of two-dimensional titanium carbide," *Science*, vol. 341, no. 6153, pp. 1502–1505, 2013.

[42] T. A. Le, N. Q. Tran, Y. Hong, and H. Lee, "Intertwined titanium carbide MXene within a 3 D tangled polypyrrole nanowires matrix for enhanced supercapacitor performances," *Chemistry A European Journal*, vol. 25, no. 4, pp. 1037–1043, 2019.

[43] M. Ghidiu, M. R. Lukatskaya, M.-Q. Zhao, Y. Gogotsi, and M. W. Barsoum, "Conductive two-dimensional titanium carbide 'clay' with high volumetric capacitance," *Nature*, vol. 516, no. 7529, pp. 78–81, 2014.

[44] M. Naguib, V. N. Mochalin, M. W. Barsoum, and Y. Gogotsi, "Two-dimensional materials: 25th anniversary article: MXenes: a new family of two-dimensional materials (Adv. Mater. 7/2014)," *Advanced Materials*, vol. 26, no. 7, pp. 982–982, 2014.

[45] G. Gao, A. P. O'Mullane, and A. Du, "2D MXenes: a new family of promising catalysts for the hydrogen evolution reaction," *ACS Catalysis*, vol. 7, no. 1, pp. 494–500, 2017.

[46] C. Ling, L. Shi, Y. Ouyang, and J. Wang, "Searching for highly active catalysts for hydrogen evolution reaction based on O-terminated MXenes through a simple descriptor," *Chemistry of Materials*, vol. 28, no. 24, pp. 9026–9032, 2016.

[47] J. Pang, R. G. Mendes, A. Bachmatiuk et al., "Applications of 2D MXenes in energy conversion and storage systems," *Chemical Society Reviews*, vol. 48, no. 1, pp. 72–133, 2019.

[48] H. He, Y. Chen, C. Yang, L. Yang, Q. Jiang, and H. Huang, "Constructing 3D interweaved MXene/graphitic carbon nitride nanosheets/graphene nanoarchitectures for promoted electrocatalytic hydrogen evolution," *Journal of Energy Chemistry*, vol. 67, pp. 483–491, 2022.

[49] B. Shen, H. Huang, Y. Jiang, Y. Xue, and H. He, "3D interweaving MXene-graphene network-confined Ni-Fe layered double hydroxide nanosheets for enhanced hydrogen evolution," *Electrochimica Acta*, vol. 407, article 139913, 2022.

[50] H. Huang, Y. Xue, Y. Xie et al., "MoS_2 quantum dot-decorated MXene nanosheets as efficient hydrogen evolution electrocatalysts," *Inorganic Chemistry Frontiers*, vol. 9, no. 6, pp. 1171–1178, 2022.

[51] C. Yang, H. Huang, H. He, L. Yang, Q. Jiang, and W. Li, "Recent advances in MXene-based nanoarchitectures as electrode materials for future energy generation and conversion applications," *Coordination Chemistry Reviews*, vol. 435, article 213806, 2021.

[52] L. Zhao, B. Dong, S. Li et al., "Interdiffusion reaction-assisted hybridization of two-dimensional metal–organic frameworks and $Ti_3C_2T_x$Nanosheets for electrocatalytic oxygen evolution," *ACS Nano*, vol. 11, no. 6, pp. 5800–5807, 2017.

[53] K. Lim, A. Handoko, S. K. Nemani et al., "Rational design of two-dimensional transition metal carbide/nitride (MXene) hybrids and nanocomposites for catalytic energy storage and conversion," *ACS Nano*, vol. 14, no. 9, pp. 10834–10864, 2020.

[54] T. A. Le, Q. V. Bui, N. Q. Tran et al., "Synergistic effects of nitrogen doping on MXene for enhancement of hydrogen evolution reaction," *ACS Sustainable Chemical Engineering*, vol. 7, no. 19, pp. 16879–16888, 2019.

[55] B. Ding, W.-J. Ong, J. Jiang, X. Chen, and N. Li, "Uncovering the electrochemical mechanisms for hydrogen evolution reaction of heteroatom doped M_2C MXene (M=Ti, Mo)," *Applied Surface Science*, vol. 500, article 143987, 2020.

[56] K. D. Fredrickson, B. Anasori, Z. W. Seh, Y. Gogotsi, and A. Vojvodic, "Effects of applied potential and water intercalation on the surface chemistry of Ti_2C and Mo_2C MXenes," *Journal of Physical Chemistry C*, vol. 120, no. 50, pp. 28432–28440, 2016.

[57] M. Ghidiu, J. Halim, S. Kota, D. Bish, Y. Gogotsi, and M. W. Barsoum, "Ion-exchange and cation solvation reactions in Ti_3C_2 MXene," *Chemistry of Materials*, vol. 28, no. 10, pp. 3507–3514, 2016.

[58] J. Jia, T. Xiong, L. Zhao et al., "Ultrathin N-doped Mo_2C nanosheets with exposed active sites as efficient electrocatalyst for hydrogen evolution reactions," *ACS Nano*, vol. 11, no. 12, pp. 12509–12518, 2017.

[59] J. Halim, K. M. Cook, M. Naguib et al., "X-ray photoelectron spectroscopy of select multi-layered transition metal carbides (MXenes)," *Applied Surface Science*, vol. 362, pp. 406–417, 2016.

[60] E. B. Simsek, "Solvothermal synthesized boron doped TiO_2 catalysts: photocatalytic degradation of endocrine disrupting compounds and pharmaceuticals under visible light irradiation," *Applied Catalysis B: Enviromental*, vol. 200, pp. 309–322, 2017.

[61] N. Patel, A. Dashora, R. Jaiswal et al., "Experimental and theoretical investigations on the activity and stability of substitutional and interstitial boron in TiO_2Photocatalyst," *Journal of Physical Chemistry C*, vol. 119, no. 32, pp. 18581–18590, 2015.

[62] E. Finazzi, C. Di Valentin, and G. Pacchioni, "Boron-doped anatase TiO_2: pure and hybrid DFT calculations," *Journal of Physical Chemistry*, vol. 113, no. 1, pp. 220–228, 2009.

[63] X. Liang, Y. Rangom, C. Y. Kwok, Q. Pang, and L. F. Nazar, "Interwoven MXene nanosheet/carbon-nanotube composites as Li–S cathode hosts," *Advanced Materials*, vol. 29, no. 3, article 1603040, 2017.

[64] Y. Lu, Z. Zhou, P. Sit, Y. Shen, K. Li, and H. Chen, "X-Ray photoelectron spectroscopy characterization of reactively sputtered Ti-B-N thin films," *Surface and Coatings Technology*, vol. 187, no. 1, pp. 98–105, 2004.

[65] N. Lu, X. Quan, J. Li, S. Chen, H. Yu, and G. Chen, "Fabrication of boron-doped TiO_2 Nanotube array electrode and investigation of its photoelectrochemical capability," *Journal of Physical Chemistry C*, vol. 111, no. 32, pp. 11836–11842, 2007.

[66] R. B. Rakhi, B. Ahmed, M. N. Hedhili, D. H. Anjum, and H. N. Alshareef, "Effect of postetch annealing gas composition on the structural and electrochemical properties of Ti_2CT_xMXene electrodes for supercapacitor applications," *Chemistry of Materials*, vol. 27, no. 15, pp. 5314–5323, 2015.

[67] M. Bat-Erdene, M. Batmunkh, B. Sainbileg et al., "Highly dispersed Ru nanoparticles on boron-doped $Ti_3C_2T_x$ (MXene) nanosheets for synergistic enhancement of electrocatalytic hydrogen evolution," *Small*, vol. 17, no. 38, article 2102218, 2021.

[68] W. Ma, D. Liu, F. Gao et al., "P-doped $MoS_2/Ni_2P/Ti_3C_2T_x$ heterostructures for efficient hydrogen evolution reaction in alkaline media," *Journal of American Ceramic Society*, vol. 105, no. 10, pp. 6096–6104, 2022.

[69] J. Wang, Y. Liu, and G. Yang, "Cobalt decorated ultra-thin Ti_3C_2 MXene electrocatalyst for high-efficiency hydrogen evolution reaction," *Material Research Express*, vol. 6, article 025056, 2018.

[70] I. Ashraf, S. Ahmad, S. Rizwan, and M. Iqbal, "Fabrication of $Ti_3C_2@MoO_3$ nanocomposite as an electrode material for highly efficient and durable water splitting system," *Fuel*, vol. 299, article 120928, 2021.